Thermal and compositional anomalies beneath the North American continent

S. Godey,[1] F. Deschamps, and J. Trampert
Faculty of Earth Sciences, Utrecht University, Utrecht, Netherlands

R. Snieder
Department of Geophysics, Colorado School of Mines, Golden, Colorado, USA

Received 23 October 2002; revised 1 May 2003; accepted 24 September 2003; published 24 January 2004.

[1] The thermal and compositional structure of the upper mantle beneath the North American continent is investigated using a joint inversion of seismic velocities and density perturbations. The velocity data consist of a new regional shear wave velocity model of North America and the Caribbean region obtained by surface wave tomography. The density data are estimated using a relative density-to-shear velocity scaling factor computed for continents by combining regionally filtered seismic and gravity data. We express the mineralogical variations in the mantle in terms of the global volumic fraction of iron, the parameter which has the strongest influence on density and velocity. The inferred thermal and iron content anomalies are well constrained by the data and show an age dependence down to a depth of 230 ± 50 km. Below the North American craton, the mantle is colder than average and depleted in iron. Maximum values are found at 100 km with $\overline{\delta T} = -440$ K and $\overline{\delta \mathrm{Fe}} = -4\%$, relative to the average mantle. These chemical and thermal characteristics induce opposite buoyancy forces which could explain the longevity of cratonic lithosphere. In stable continental areas, the signal is of lower amplitudes ($\overline{\delta T} = -280$ K and $\overline{\delta \mathrm{Fe}} = -2.5\%$ at 100 km). Beneath the western Cordillera, a tectonically active region, we see no significant thermal or chemical anomaly. *INDEX TERMS:* 7218 Seismology: Lithosphere and upper mantle; 7260 Seismology: Theory and modeling; 8124 Tectonophysics: Earth's interior—composition and state (1212); 9350 Information Related to Geographic Region: North America

Citation: Godey, S., F. Deschamps, J. Trampert, and R. Snieder (2004), Thermal and compositional anomalies beneath the North American continent, *J. Geophys. Res.*, *109*, B01308, doi:10.1029/2002JB002263.

1. Introduction

[2] Recent global and regional tomographic models display a high correlation between surface tectonic features and seismic velocities down to moderate depths. In addition, velocity anomalies correlate well with the age of surface materials [e.g., *Polet and Anderson*, 1995; *Ekstrom*, 2000]. A challenge is still to infer the exact thermal and chemical variations that are responsible for the observed seismic velocity anomalies. Important questions, such as the extent of continental roots and their origin are still debated. *Jordan* [1975] first associated high seismic velocity beneath cratons with low temperature and a specific petrology. The analysis of surface xenoliths [e.g., *Rudnick and Nyblade*, 1999], which are direct samples of the Earth's mantle, suggest large compositional variations in the cratonic lithosphere, which would allow the longevity of cratons [*Jordan*, 1979; *Anderson*, 1979]. If high velocities are manifestations of purely thermal variations, the density would increase and subsidence would occur as a consequence of negative buoyancy forces. As the topography does not show signs of such a subsidence, compositional variations are needed to balance the thermal effect.

[3] *Jordan* [1979] suggested that cratons extent down to a depth of 400 km. More recent studies report smaller thicknesses, up to 250 km [*Röhm et al.*, 2000; *Rudnick and Nyblade*, 1999; *Forte and Perry*, 2000; *Artemieva and Mooney*, 2001; *Griffin et al.*, 1999]. Seismic velocities are primarily sensitive to temperature variations [*Duffy and Anderson*, 1989; *Goes et al.*, 2000], and as a consequence, investigation of the continental thermal structure using seismic tomography alone could not isolate compositional variations [e.g., *Yan et al.*, 1989]. Combining heat flow data and seismic tomography, *Röhm et al.* [2000] estimated the thickness of the thermal lithosphere but speculated that compositional variations could influence their results. Beneath cratonic areas, chemical depletion could further explain some inconsistencies observed in seismic data [*Goes and van der Lee*, 2002; *Humphreys and Dueker*, 1994]. *Forte et al.* [1995] showed that the ocean-continent difference in seismic tomography is not purely thermal in origin, but to infer the mineralogical perturbations, addi-

[1] Now at European Mediterranean Seismological Centre, Bruyères-le-Châtel, France.

0148-0227/04/2002JB002263$09.00

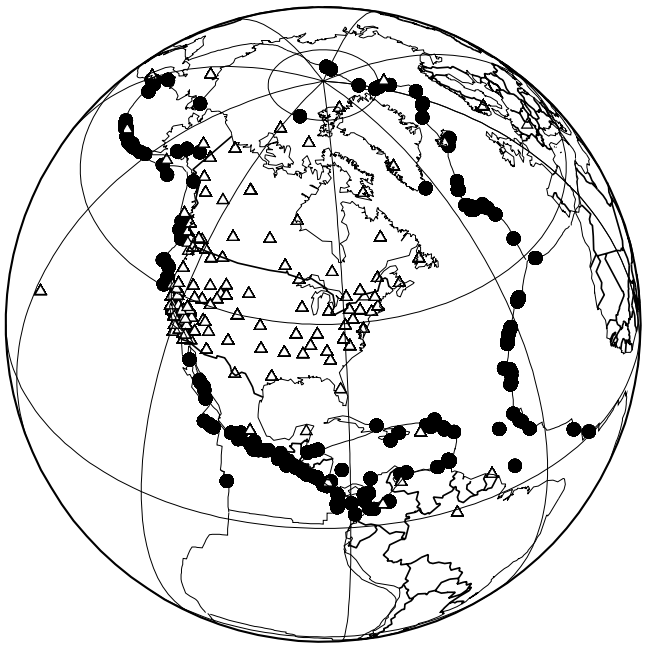

Figure 1. Distribution of earthquakes (circles) and stations (triangles).

tional data are needed. Using gravity anomalies to constrain density, recent studies [*Forte and Perry*, 2000; *Deschamps et al.*, 2002] could invert shear velocity and density for anomalies of temperature and composition. In this paper, we construct a regional tomographic model of *S* wave velocity anomalies for North America. We then use this model and the method of *Deschamps et al.* [2002] to infer distributions of temperature and composition below the North American continent.

2. Shear Wave Velocity Model

[4] Many tomographic models beneath the north American continent have been proposed. They focus on different length scales (local to regional), and the type of data varies from body waves and surface waves to full waveforms. A recent overview of most of these results is given by *Goes and van der Lee* [2002]. Guided by the fact that surface waves provide the best depth resolution, and that the step via classical phase velocity maps allows to incorporate the greatest amount of waveforms, we propose a new shear wave velocity model. Our focus is to achieve the most homogeneous resolution needed to make an interpretation in terms of temperature and composition, rather than the best possible local resolution given our data set.

2.1. Data

[5] We measured phase velocities of fundamental mode Rayleigh waves from 207 events recorded by 142 global (GSN) and regional (CNSN, USNSN, BDSN, Terrascope and Geoscope) stations between 1995 and 1999. The phase velocity measurements are obtained automatically, using the nonlinear waveform inversion of *Trampert and Woodhouse* [1995]. The phase and amplitude as a function of frequency of each seismogram are expanded in terms of B splines. A smoothing constraint is applied to solve the 2π phase ambiguity, particularly at short periods. The necessary starting model is a global phase velocity model of *Trampert and Woodhouse* [1995]. The automatic selection resulted in 7700 phase velocity measurements. The period range extends from 40 s to 150 s, and the same data coverage is obtained for all periods. Focal mechanisms are taken from the Harvard centroid moment tensor solutions. Earthquake depths are limited to 100 km, and the magnitudes vary from 4.9 to 7.0. The area mapped in the present work is bounded by the Arctic region in the north, the Caribbean basin in the south, the Aleutian islands in the east, and the Mid-Atlantic Ridge in the west. The station and source geometry is displayed in Figure 1, and the resulting ray density is shown in Figure 2. We use the method of *Barmin et al.* [2001] to construct phase velocity maps and define a grid of $2^\circ \times 2^\circ$ spacing, which is not to be confused with the achieved lateral resolution (see below), leading to 2569 grid points. Over the inversion region, the cell area, defined by four neighboring points, does not vary by more than 10%. Bilinear interpolation is used to evaluate velocities between the three nearest nodes of the grid.

[6] PREM [*Dziewonski and Anderson*, 1981], used as a reference model in the present study, has a constant crustal thickness, but short-period surface waves are very sensitive to crustal variations. To get an unbiased view of the underlying mantle, a crustal correction is necessary. Correcting the path averaged measurements is less dependent on the local crustal details than correcting the phase velocity maps, and thus more robust. Given the resolution we can achieve with our data coverage (see below), we used CRUST5.1 [*Mooney et al.*, 1998], together with topography and bathymetry to make an exact calculation of the path averaged crustal contribution, which we subtracted from each measurement at each period.

2.2. Phase Velocity Map and Resolution

[7] To obtain equal resolution in all phase velocity maps, we applied the same Laplacian regularization at all periods.

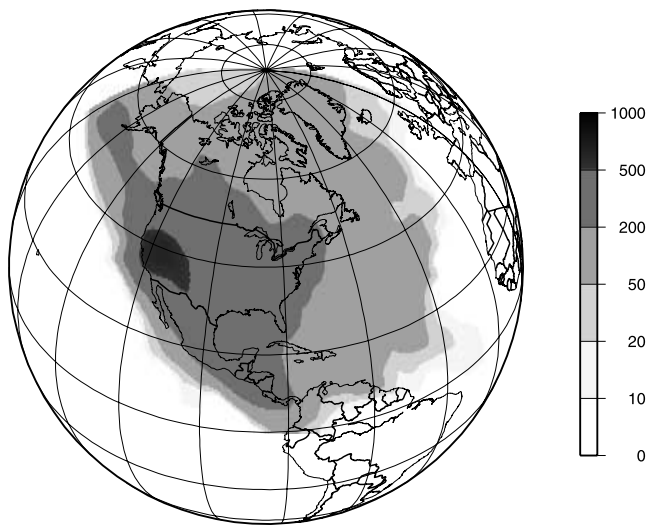

Figure 2. Ray path density, defined as the number of rays intersecting a $2^\circ \times 2^\circ$ cell.

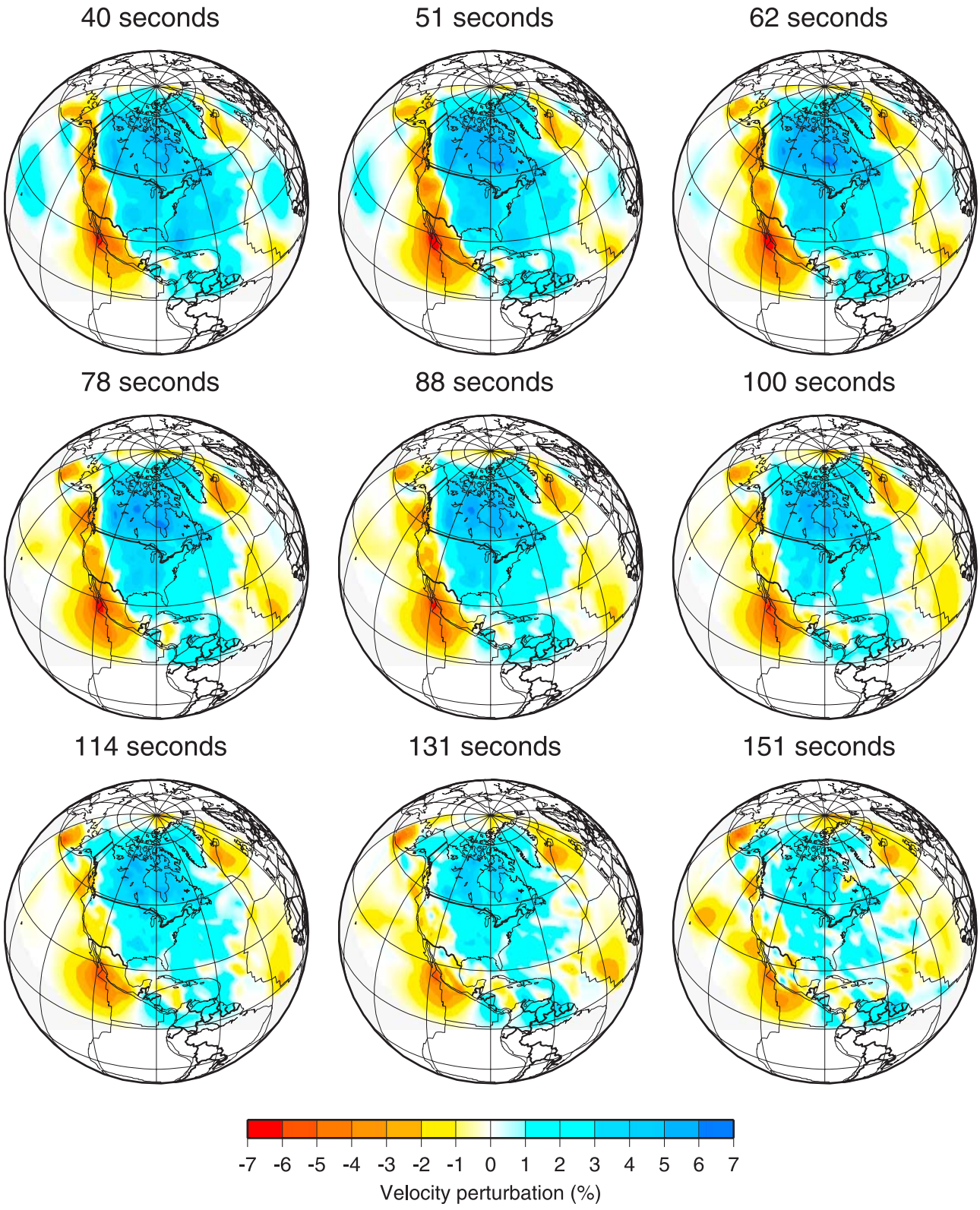

Figure 3. Phase velocity maps for North America and the Caribbean used as input data in the inversion for *S* wave velocities. The velocities are given in percent relative to PREM.

We therefore avoid artifacts in the depth inversion. The estimated phase velocity model is given by

$$\hat{m} = \left(G^T G + \alpha^2 W\right)^{-1} G^T d, \quad (1)$$

where W is a Laplacian regularization operator.

[8] We chose to slightly overdamp the inversion so that robust features are imaged (Figure 3). The spatial resolution is quantified by the resolution spreading function [*Backus and Gilbert*, 1967] and the diagonal elements of the resolution matrix (Figure 4).

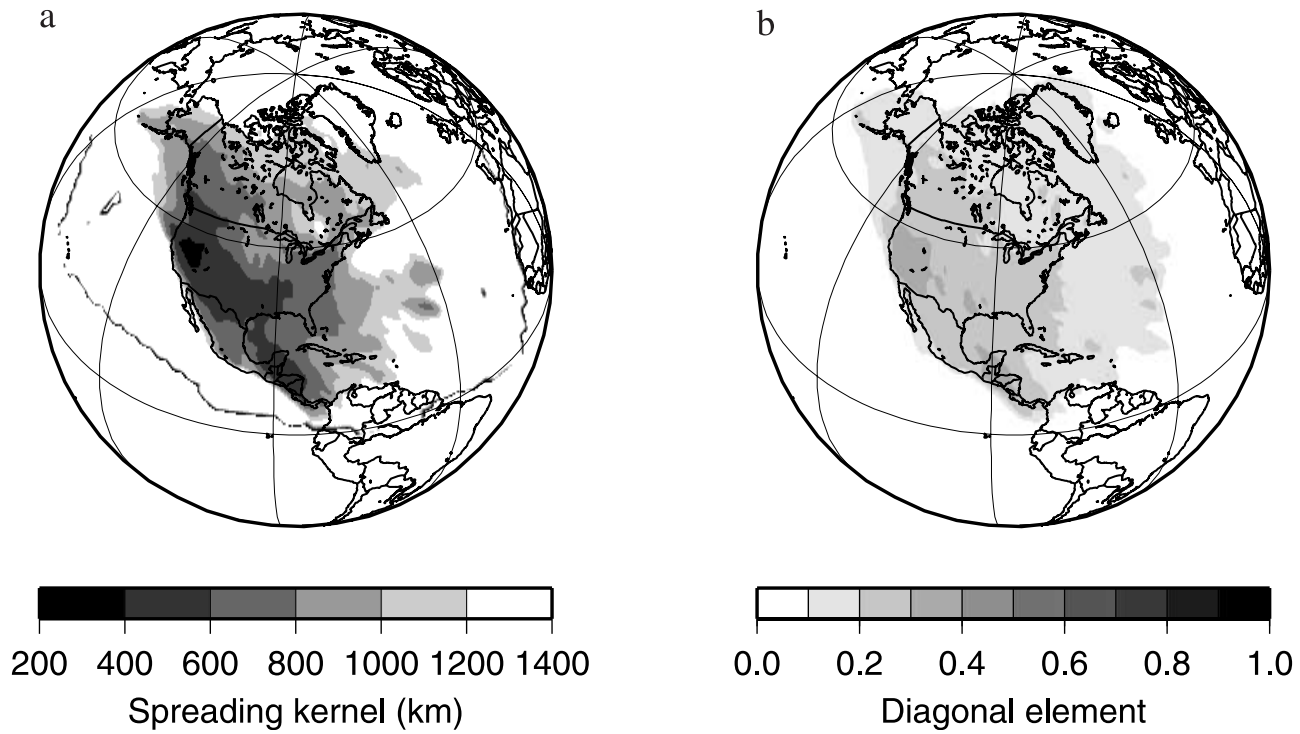

Figure 4. Distribution of (a) the resolution spreading function and (b) the value of the diagonal elements of the resolution matrix for the phase velocity map of 100 s.

$$K_i = \frac{24}{dr} \frac{\sum_{k=1}^{N} D_{ki}^2 R_{ki}^2}{\sum_{k=1}^{N} R_{ki}^2}, \tag{2}$$

with

$$R = \left(G^T G + \alpha^2 W\right)^{-1} G^T G, \tag{3}$$

where R_{ki} is the resolution matrix element (k, i), D_{ki} the distance in kilometers between the parameter node i and the nodes k and dr is the grid spacing 220 km.

[9] The parameter K reflects how far the off-diagonal elements of the resolution matrix spread around each model point. For poorly constrained parameters, the spreading function has large values, whereas for a perfectly defined parameter ($R = I$) the K_i are equal to zero. The damping parameter we have chosen allows an average lateral resolution of 800 km, the best resolution (400 km) being obtained in the western United States. Of course, for regions with lower ray path coverage, the spreading function displays higher values, i.e., lower resolution. The resulting phase velocity maps explain the data with variance reductions of about 90% at short periods and 50% at long periods.

2.3. *S* Wave Velocity Modeling

[10] The Earth's shear velocity structure as a function of depth is derived by combining the phase velocity maps computed for different periods with the same lateral resolution. At each point of the grid, the inverse problem is specified by the data, the local phase velocities ($\delta c/c$), and the model corresponding to a local depth profile for S wave velocity ($\delta v_s/v_s$) relative to PREM. Strictly speaking, the local phase velocities are sensitive to radial and azimuthal anisotropy. *Trampert and Woodhouse* [2003] have clearly shown that neglecting azimuthal anisotropy has only an effect on the shortest wavelength structure, which we are not mapping here. Neglecting transverse anisotropy and given currently known values for its deviation from PREM in the region will bias $\delta \ln v_s$ by 0.3% but may reach locally

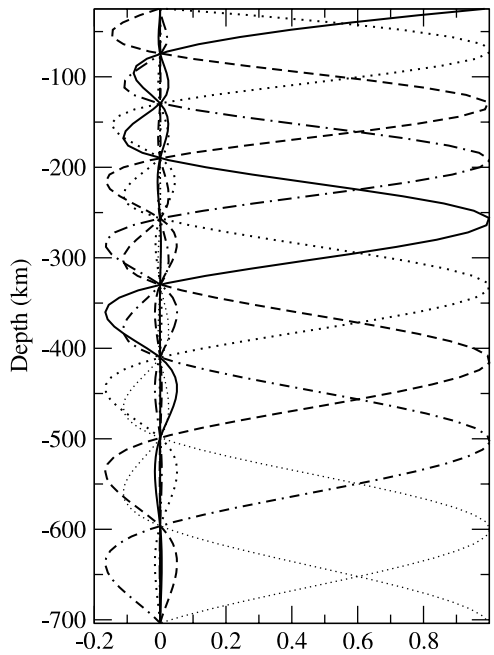

Figure 5. Spline functions used to parameterize the S wave velocity as a function of depth.

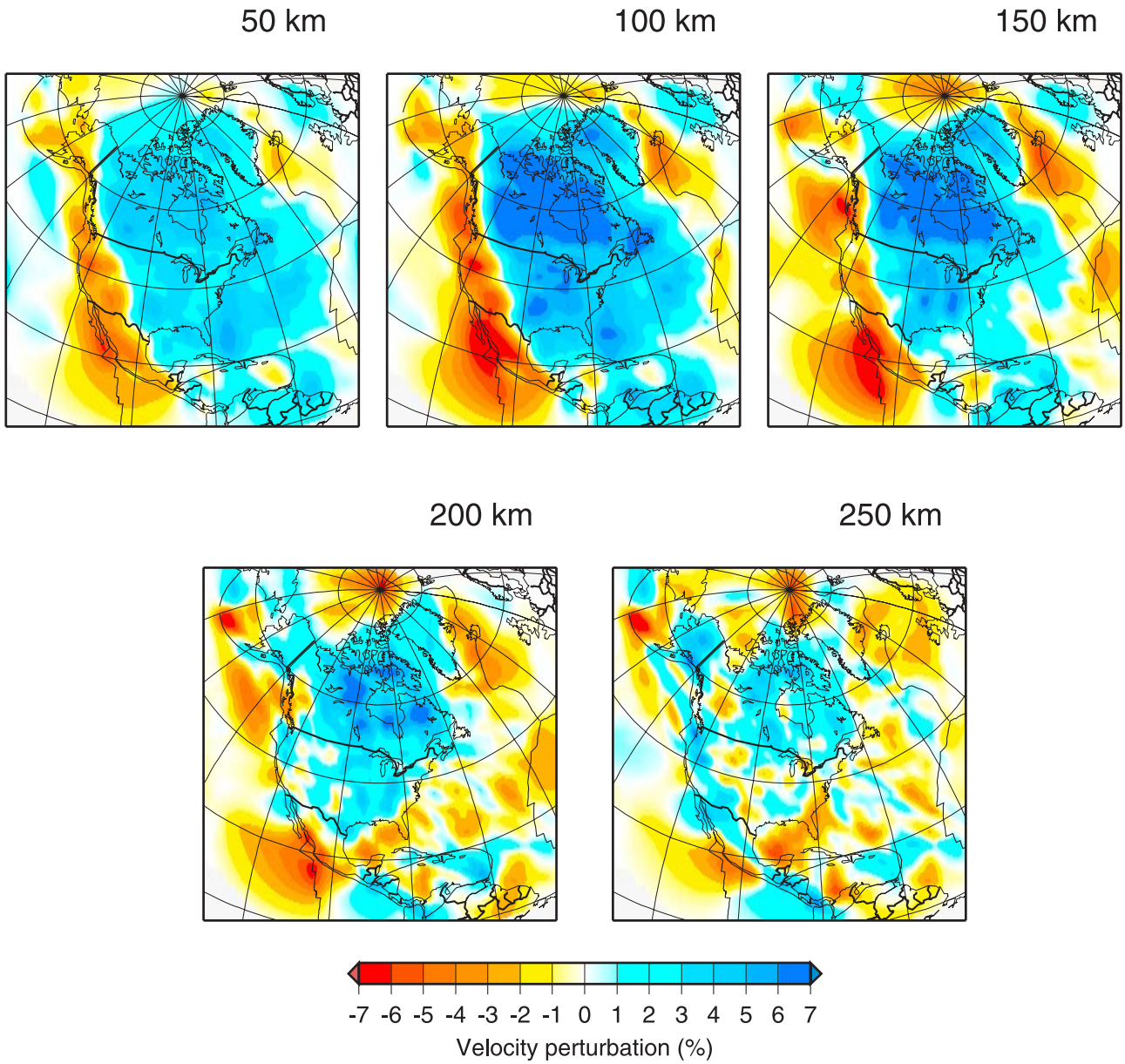

Figure 6. Relative *S* wave velocity perturbation model for depths of 50–250 km.

1.5%. Given the overall strength of the models and errors associated with the thermochemical interpretation, neglecting anisotropy has a minor effect on our conclusions. The relation between data and model assuming isotropy is then

$$\frac{\delta c}{c}(\theta,\phi) = \int_0^R K_s(r)\frac{\delta v_s}{v_s}(r,\theta,\phi)dr + \int_0^R K_p(r)\frac{\delta v_p}{v_p}(r,\theta,\phi)dr + \int_0^R K_\rho(r)\frac{\delta \rho}{\rho}(r,\theta,\phi)dr, \quad (4)$$

where K_s, K_p, K_ρ are the sensitivities of surface waves to *S* wave velocity (v_s), *P* wave velocity (v_p) and density (ρ), respectively. R is the radius of the Earth, θ and ϕ are the latitude and longitude of the grid point considered. As Rayleigh waves are primarily sensitive to *S* and *P* wave velocity, we further neglect the sensitivity to density (third term of equation (4)). We assumed a constant ratio between *S* and *P* wave velocities and used the value proposed by *Robertson and Woodhouse* [1997], $\delta \ln v_s / \delta \ln v_p = 1.6$, which was inferred from travel time data. Because Rayleigh waves are not very sensitive to v_p and ρ, the exact scaling parameter hardly matters for the resulting v_s model. Relation (4) is thus reduced to a term containing $\delta \ln v_s$ only. For our North American data set, which consists of phase velocities between 40 and 150 s, *S* wave velocity perturbations between 60 and 260 km can be retrieved. We expand our model as a function of depth in terms of spline functions. For a given grid point, the *S* wave velocity is

$$m(r,\theta,\phi) = \frac{\delta v_s}{v_s}(r,\theta,\phi) = \sum_{i=1}^{N} b_i(\theta,\phi)B_i(r), \quad (5)$$

where the functions $B_i(r)$ are the cubic splines as a function of depth, and b_i the coefficients we invert for. We used 10 equally spaced splines (Figure 5).

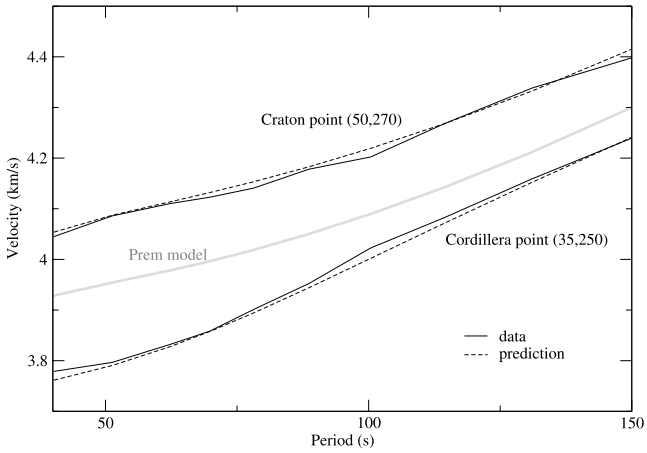

Figure 7. Phase velocity dispersion curves observed (solid line) and predicted (dashed line) by our shear velocity model for two characteristic points. Velocities are given as absolute values and are compared with PREM (grey line).

[11] A regularization term is added, which controls the smoothness of the model. The regularization operator is computed for each model point by integrating the second derivatives of the spline functions:

$$W_{ij} = \int_0^R \frac{d^2B_i(r)}{dr^2}\frac{d^2B_j(r)}{dr^2}dr. \quad (6)$$

The estimated model is obtained using a standard least squares inversion technique, which minimizes simultaneously data fit and model smoothness:

$$(Gm - d)^T(Gm - d) + \alpha^2 m^T W m. \quad (7)$$

The value of α we have chosen is such that the trace of resolution is approximately 3, or that three equivalent spline coefficients are independently resolved.

2.4. *S* Wave Velocity Model

[12] Figure 6 shows our shear wave velocity model expressed as relative perturbations from PREM. Maximum amplitudes are of the order of ±9.5% at 100 km. Interestingly, they do not decrease significantly at larger depths as observed in other studies [e.g., *Van der Lee and Nolet*, 1997; *Grand*, 1994]. The difference is most likely due to different regularization schemes, rather than data constraints. The *S* wave velocity model explains the data with a variance reduction varying between 74 and 85%, depending on the period. Two representative points, one located in the tectonically active western margin (35°N, 110°W) and one in the cratonic area (50°N, 120°W), are chosen to illustrate the data fit. For both locations, we obtain a very good fit over the complete period range, with deviations less than 0.5% from the absolute velocity (Figure 7). We repeated this exercise to all our grid points and found good agreement in amplitude and location of the original phase velocity maps over the entire region, with a maximum difference locally of 1% at 100 s.

[13] Our model agrees well with observed surface tectonics. The two prominent features imaged in our model are the high velocities beneath the North American craton and the lower velocities associated with the western active Cordillera. These structures extend down to depths of 200 km and 150 km, respectively. The boundary separating the two anomalies is sharp, as seen in cross sections of Figure 8, and aligns well with the topography along the Mackenzie mountain range, in Canada, and along the Rocky mountains front, in the United States and Mexico. These anomalies are well reported in the literature and are associated with the different surface tectonic provinces. Using various methods and data sets, previous studies display however different lateral and vertical extensions of the tectonic and cratonic regions [e.g., *Bassin et al.*, 2000; *Grand*, 1994; *Van der Lee and Nolet*, 1997]. A tectonic interpretation of the main features is given by *Goes and van der Lee* [2002, and references therein].

2.5. Seismic Velocities and Surface Heat Flow

[14] Surface heat flow measurements provide additional and independent information on the thermal structure of the crust and the lithosphere. It is interesting to compare tomographic models to surface heat flow data. We used the compilation of global heat flow data by G. Masters and G. Laske (personal communication, 2002). This data set is available on http://mahi.ucsd.edu/Gabi/rem.dir/crust/heatflow.html and consists of 38,000 measurements including the earlier data of *Pollack et al.* [1993]. Figure 9 shows the correlation between our shear velocity model and the surface heat flow on a $2° \times 2°$ grid. A strong anticorrelation of the heat flow with the *S* wave velocity is observed from 60 km (average crustal thickness) to 180 km. *Röhm et al.* [2000] reported a similar result and explained it by a combination of radiogenic heat production in the crust and the thickness of the thermal lithosphere. This result suggests that thermal processes are sufficient to explain *S* wave tomography and heat flow data. It is well established that in the upper mantle, seismic velocities are mostly sensitive to temperature [*Goes and van der Lee*, 2002; *Deschamps et al.*, 2002]. This should not be understood that chemical variations are absent, but rather that other data, such as density variations, are required to detect them.

3. Thermal and Compositional Structure

[15] To infer thermal and compositional variations from our v_s model, we propose to add density variations as an additional constraint. It is currently very difficult to obtain independent density variations from seismology or other data. We therefore follow a classical approach, which constrains density anomalies from observed gravity anomalies using an appropriate scaling to velocity. We can then invert the correlated density anomalies and the velocity anomalies for anomalies of temperature and composition. This requires a careful equation of state modeling and the most recent results of mineral physics.

3.1. Constraining the Density

[16] To constrain density anomalies, we have inverted the global *S* wave velocity anomalies S16RLBM [*Woodhouse and Trampert*, 1995] and the nonhydrostatic gravity anomalies derived from EGM96 [*Lemoine et al.*, 1998] for a radial profile of the relative density-to-shear velocity ratio,

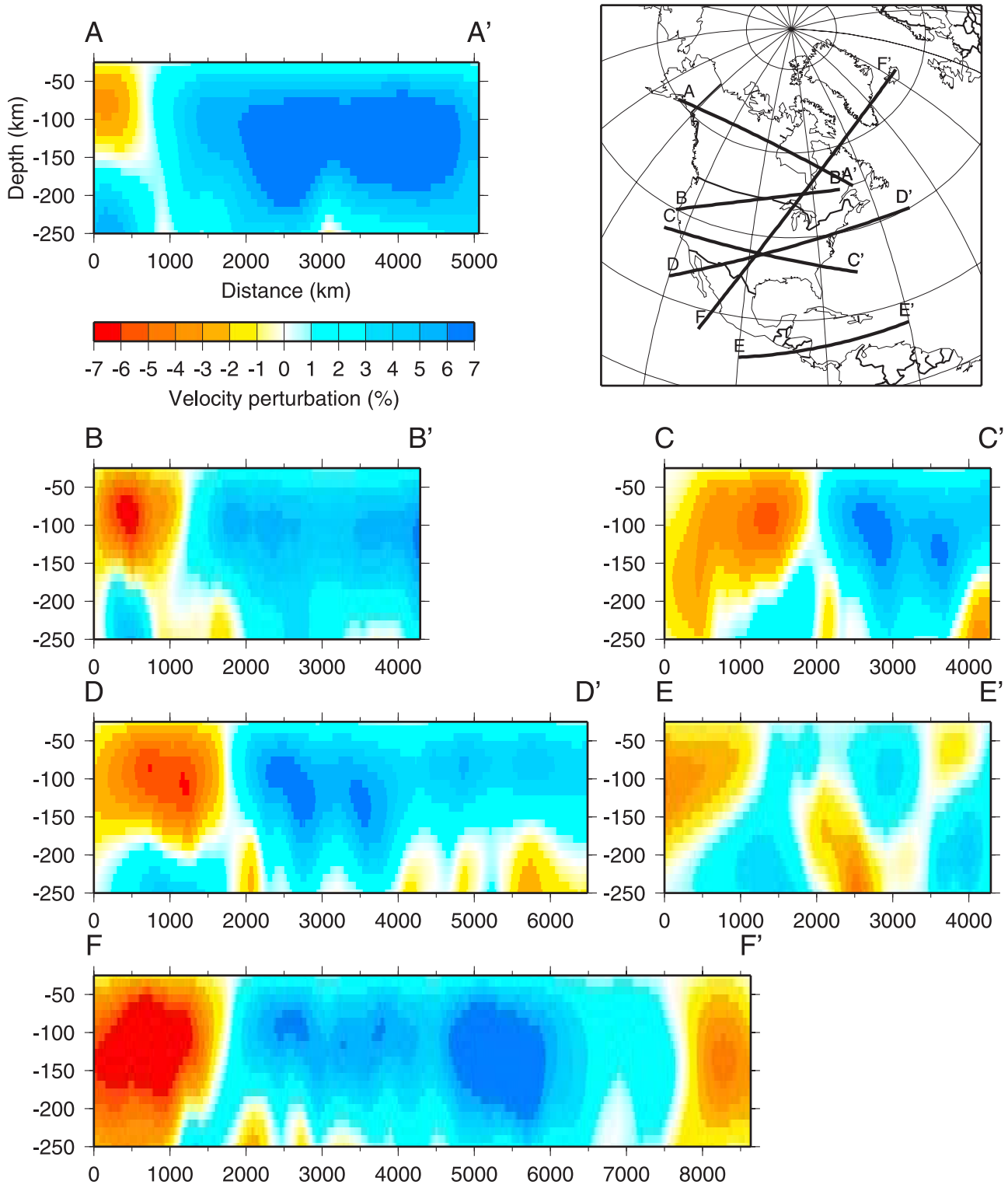

Figure 8. Cross sections through the *S* wave velocity model of Figure 6. The location of the cross sections are shown on the map (top right).

$$\zeta(r,\theta,\phi) \equiv \frac{\delta \ln \rho(r,\theta,\phi)}{\delta \ln v_s(r,\theta,\phi)}. \quad (8)$$

Regionally dependent ratios can be computed from existing data, and the scaling factor used in the present study (Figure 10) is for subcontinental mantle [*Deschamps et al.*, 2001].

[17] Observed gravity anomalies integrate the density anomalies over depth. For each degree ℓ of the spherical harmonic expansion, the gravity anomalies can be written

$$\delta g_\ell(\theta,\phi) = \int_{r_{CMB}}^{R} K_\ell(r)\delta\rho_\ell(r,\theta,\phi)dr \quad (9)$$

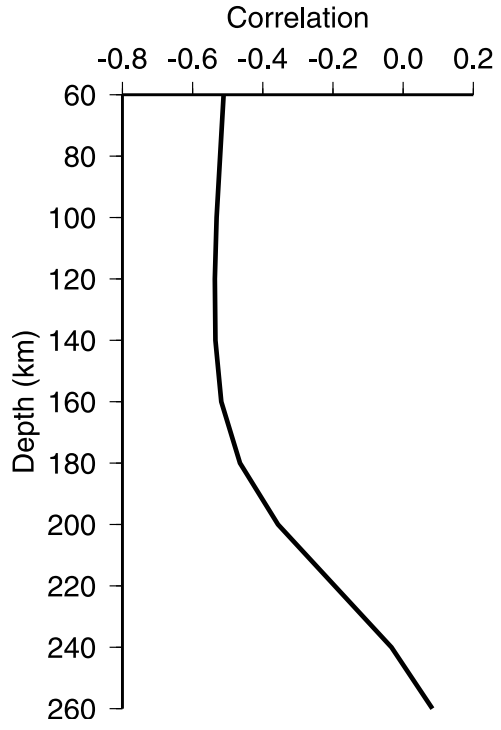

Figure 9. Correlation between *S* wave velocity at a given depth and surface heat flow for North America.

$$K_\ell(r) = \frac{3g_0}{\bar{\rho}R}\frac{(\ell-1)}{(2\ell+1)}G_\ell(r), \tag{10}$$

where R and $\bar{\rho}$ are the Earth's radius and average density, r_{CMB} is the radius of the core, and g_0 is the surface gravity acceleration. The functions G_ℓ(r) are the geoid kernels, i.e., the geoid response to density anomalies located at depth, computed following the method of *Forte and Peltier* [1991]. Introducing equation (8) into equation (9) and filtering each member of equation (9) between spherical harmonic degrees ℓ_1 and ℓ_2, one obtains a linear relation between gravity anomalies, velocity anomalies, and the scaling factor ζ. We solve this equation for radial profiles of ζ in the suboceanic and subcontinental mantle, assuming that ζ does not vary laterally within each of these two regions. Inversions are regularized with a smoothness constraint, the amount of smoothness being controlled by a damping factor. Results depend on a number of parameters that it is important to choose correctly.

[18] First, we filtered S16RLBM and EGM96 to remove the long-wavelength gravity anomalies, which originate from deep mantle structure. Because geoid kernels for degrees 2 to 10 have nonnegligible values throughout the mantle, we only kept degrees 11 to 16 to compute the scaling factor in Figure 10. Interestingly, tests suggested that low degrees do not significantly influence the scaling factor in the upper 400 km [*Deschamps et al.*, 2001]. In the lower mantle, filtering strongly influences the obtained ratio.

[19] Second, geoid kernels depend strongly on the viscosity profile of the mantle. The later is still a mater of debate, and any choice could appear arbitrary. However, for degrees $\ell \geq 10$, geoid kernels peak in the uppermost mantle ($z \leq 200-300$ km) whatever the viscosity profile used, and have negligible values from z = 1000 km depth down to the bottom of the mantle. As a result, down to z = 400 km depth, the scaling factor is not sensitive to the viscosity profile [*Deschamps et al.*, 2001]. At greater depths, of course, major differences appear, depending on the viscosity profile, which prevents us from constraining deep Earth density with our scaling factor. In the present study, we built the geoid kernels using a viscosity profile that fit both the long-wavelength gravity anomalies and the postglacial uplift [*Mitrovica and Forte*, 1997].

[20] The scaling factor thus depends on the viscosity profile and spectral filtering, but most of the differences concern the deep mantle. At shallower depths ($z \leq 400$ km), differences are small. We also checked that the regularization of the inversion, which is always subjective, does not significantly change the shape and amplitude of $\zeta(r)$ [*Deschamps et al.*, 2001]. The main source of uncertainty stems from the uncertainty in the tomographic model. We assumed reasonable errors on δlnv_s [*Deschamps et al.*, 2001] and calculated the corresponding range of ratios shown in Figure 10.

[21] The density anomalies inferred from the scaling factor are, by definition, correlated to the velocity anomalies. Additional density anomalies, and therefore additional temperature and compositional anomalies, which are not correlated to the velocity could well be present. Currently, we cannot map these contributions. We believe, however, that most of the density anomalies are correlated to the velocity anomalies, because the gravity anomalies reconstructed from equation (9) and the correlated density

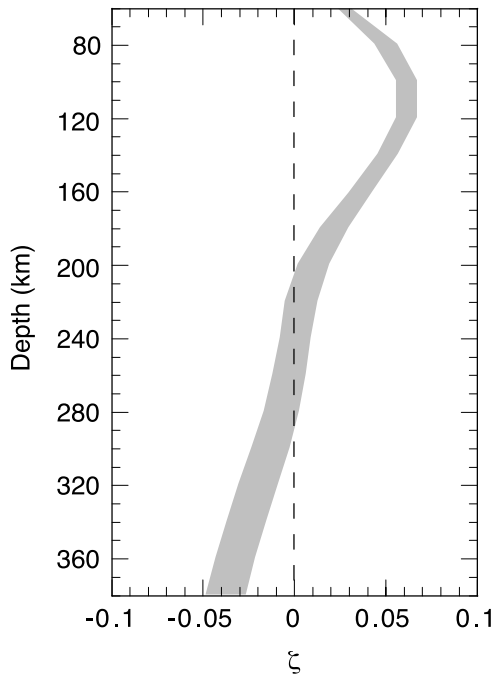

Figure 10. Radial profile of the scaling factor (ζ) for the subcontinental upper mantle. The shaded area represents a range of possible values for ζ and covers one standard deviation around the average value. The standard deviation is estimated at each depth by simulating random errors in the global *S* wave velocity model S16RLBM.

Table 1. Volumic Fraction of Minerals in the Reference Petrological Model (Pyrolite)

Mineral	Volumic Fraction, %
Olivine	61.7
Clinopyroxene	13.3
Orthopyroxene	5.2
Garnet	15.3
Jadeite	4.5

anomalies fit the observed gravity anomalies within two standard deviations.

3.2. Modeling Approach

[22] Numerical methods to compute upper mantle density and seismic velocities from mineral physics data, given temperature, pressure and petrology, are now well established [e.g., *Duffy and Anderson*, 1989]. Such methods allow to calculate relative derivatives (or sensitivities) of seismic velocity and density to temperature and composition. The method we used here is fully described by *Deschamps et al.* [2002]. The density and elastic moduli of a given mineral at ambient temperature and pressure are first extrapolated to foot temperature T_f, following Grüneisen theory. In a second step, they are adiabatically projected at pressure P, following a Birch-Munaghan equation of state to third order. The density and elastic moduli of the aggregate are then obtained by averaging over all individual minerals according to their abundance in the petrological reference model. Before extrapolations to high temperature and pressure, and if data are available, we have corrected the density and elastic parameters of individual minerals for their iron dependence. In the upper mantle, anelasticity significantly influences the reconstruction of seismic velocities [*Karato*, 1993; *Jackson*, 2000]. We accounted for this effect using a quality factor model as described by *Goes et al.* [2000] (model Q1). The presence of partial melt or fluids in the mantle may also influence the reconstruction of seismic velocities. However, the consequences of these effects are difficult to estimate, because they depend on the geometry and interconnection of the melt inclusions [*Hammond and Humphreys*, 2000]. In addition, partial melt is occurring locally. The strong anomalies of temperature and composition that partial melt may require would have a negligible effect on our regional mean values of temperature and compositional variations. In this study, we have therefore neglected the contribution of partial melt. Water effects, which modify primarily anelasticity are also neglected. The average mineralogical composition of the mantle is an important parameter in the computation of sensitivities for velocity and density, but it is still not accurately known. To account for this uncertainty, we have considered a large number of average compositions by varying the volumic fraction of olivine between 57% and 67%. The other mineralogical elements are distributed in the proportion of a pyrolitic model (Table 1).

[23] From the density and S wave velocity variations, we can independently infer the perturbations of temperature and one compositional parameter. Parameterization of composition is not straightforward, as variations in several components of the rock can change density and velocity anomalies in a complicated way. To decide of the most relevant parameter, we have computed the velocity and density perturbations for temperature and three different compositional parameters: iron, garnet, and olivine content. The global volumic fraction of iron is defined by x_{Fe} = Fe/(Fe + Mg). Garnet is richer in iron than other minerals, and its variation may be redundant with those of iron. To estimate the influence of garnet, we have arbitrarily fixed the global volumic fraction of iron to 11% in all the minerals containing iron. This corresponds then to investigate the influence of the aluminium (Al_2O_4), the second most abundant element in garnet. The relative anomalies of density and velocity obtained from thermal and compositional anomalies (iron, garnet and olivine) at 100 km depth are displayed in Figure 11. From Figure 11a, we see that the relative velocities are mainly sensitives to thermal anomalies and to a lesser extent to variations in iron. An increase of 2% in velocity can be explained either by a 120 K decrease in temperature, by a 7.5% depletion in iron, or by a 15% depletion in aluminium. Seismic velocities are much less sensitive to the fraction of olivine. A perturbation of 1% in velocity is produced by more than 50% depletion in olivine. Figure 11b shows the influence of temperature and composition on density. An enrichment of 3.5% in iron induces a 1% increase in density. The same density variation is obtained with a decrease of 400 K in temperature, or

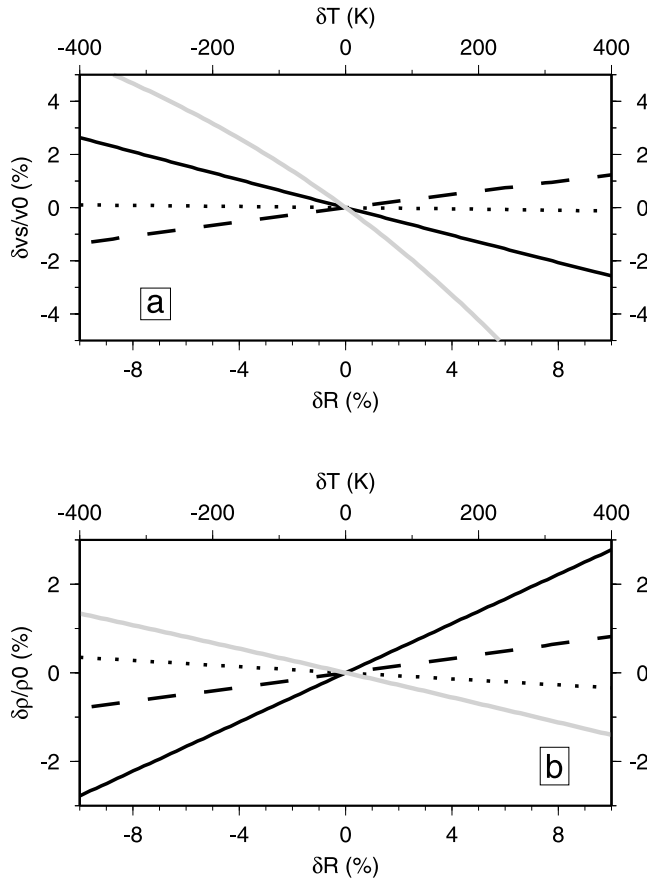

Figure 11. Relative variations of (a) velocity and (b) density as a function of variations of temperature (grey line), global volumic fraction of iron (solid line), volumic fraction of garnet (dashed line), and volumic fraction of olivine (dotted line).

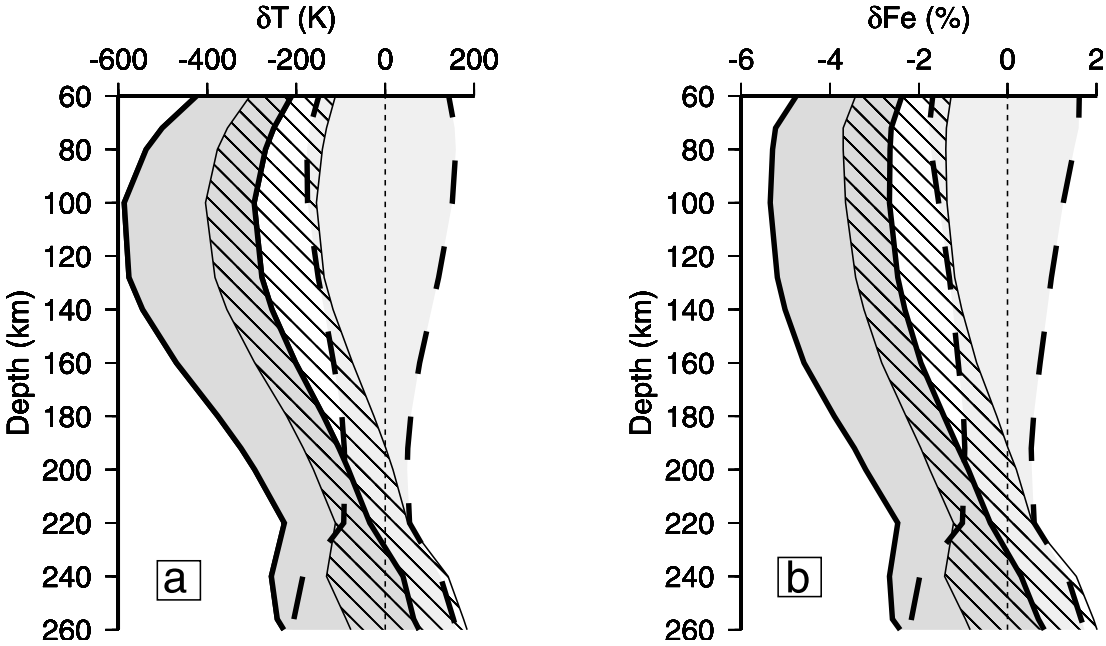

Figure 12. Profiles of (a) temperature and (b) iron anomalies for three different tectonic regions: Archean craton (dark grey), stable platform (hatched), and tectonic continent (light grey).

a 10% increase of aluminium. Among the compositional parameters, iron shows therefore the largest influence on density and velocity. Furthermore, a depletion in aluminium induces simultaneously a decrease in density and velocity. Xenolith analysis report refractory mantle composition (depleted basalts) for cratonic regions [*Schmidberger and Francis*, 1999], which are associated with high seismic velocities. This suggests that for garnet the influence of iron content is stronger than the influence of aluminium content.

[24] We finally decided to invert velocity and density anomalies for variations of temperature and iron alone, reflecting the most relevant parameters. The system to solve is defined by

$$\delta \ln v_s = A\delta T + B\delta \mathrm{Fe} \tag{11}$$

$$\delta \ln \rho = C\delta T + D\delta \mathrm{Fe} \tag{12}$$

with

$$\delta \ln \rho = \zeta \delta \ln v_s. \tag{13}$$

The coefficients A, B, C, D are the sensitivity of velocity and density to temperature (δT) and iron (δFe):

$$A = \frac{\delta \ln v_s}{\delta T}, \quad B = \frac{\delta \ln v_s}{\delta \mathrm{Fe}}, \quad C = \frac{\delta \ln \rho}{\delta T}, \quad D = \frac{\delta \ln \rho}{\delta \mathrm{Fe}} \tag{14}$$

Although $\delta \ln \rho$ is proportional to $\delta \ln v_s$, the matrix defined by A, B, C and D in equations (11) and (12) is not singular and can be inverted. Uncertainties on the tomographic model and scaling factor can propagate into the retrieved temperature and compositional structure. A bigger source of error, however, comes from uncertainties on the temperature and petrological reference models used to compute velocities and densities. We evaluated these errors by

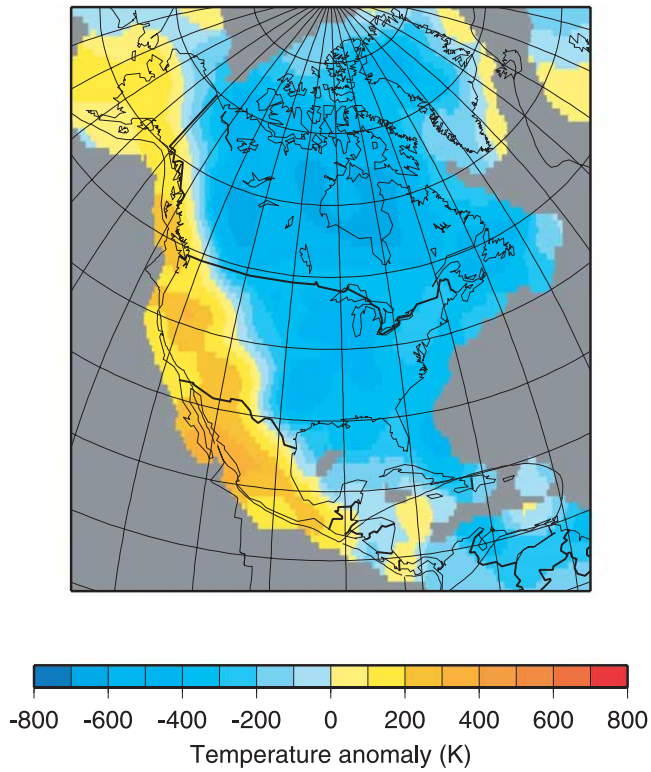

Figure 13. Map of mean temperature anomalies at 100 km depth.

sampling a reasonable range of temperature and petrological reference models. A collection of models is computed by varying the average mantle foot temperature between 800 K and 1400 K, and the olivine fraction between 36.7% and 66.7%. The global iron fraction is set to 11%. For each reference model, we calculate the velocity and density at a given depth and reject models which do not satisfy PREM within 2.5%.

[25] By exploring the mineralogical model space, we compute all possible temperature and compositional sensitivities compatible with PREM, accounting for uncertainties in the reference model. We then invert for temperature and compositional variations using this family of sensitivities. We display the results as mean temperature and compositional anomalies, together with their standard deviation.

3.3. Compositional and Thermal Profiles of the Uppermost Mantle

[26] Figure 12 displays the mean anomaly of temperature and iron and their variance (shaded area) as a function of depth and surface tectonics. We have computed profiles of δT and δFe for cratons, stable platforms and tectonically active continent, as defined by 3SMAC [*Nataf and Ricard*, 1996]. The distributions of temperature and iron anomalies are clearly related to tectonic provinces for depth shallower than 200 km. For larger depths, the difference between tectonic provinces decreases rapidly. This is partly due to the fact that the scaling factor goes to zero at these depths, hence increasing the variances in δT and δFe. An accurate determination of the depth at which the differences between tectonic provinces are cancelling requires to define profiles of the scaling factor independently for each province.

[27] Beneath tectonic continents, no significant temperature and compositional anomalies are seen. The mean values of temperature ($\overline{\delta T}$) and iron content ($\overline{\delta \mathrm{Fe}}$) are close to zero. The ranges of variation (defined as standard deviation) are small ($\sigma_{\delta T}$ = 150 K and $\sigma_{\delta \mathrm{Fe}}$ = 1%, on average). Therefore, for these regions, the mantle is close to the average, with no significant temperature or chemical differentiation. On the contrary, cratonic areas are significantly colder ($\overline{\delta T}$ varies between -200 K and -450 K for $z \leq 200$ km) and depleted in iron ($\overline{\delta \mathrm{Fe}}$ varies from -2% to -4% for $z \leq 200$ km), in comparison with an average mantle. From 60 to 200 km, the average variations are close to $\sigma_{\delta T}$ = 120 K and $\sigma_{\delta \mathrm{Fe}}$ = 1.3%. The maximum iron depletion and temperature anomaly is observed at 100 km depth with $\overline{\delta T} = -440$ K and $\overline{\delta \mathrm{Fe}} = -4\%$. Below 230 km depth, positive values of temperature and iron anomalies cannot be excluded. Defining the depth extent of cratons by the layer in which temperature and iron anomalies are negative within one standard deviation, the North American craton would be 230 ± 50 km thick. The uncertainty is given by the vertical resolution of tomographic models. The profile obtained below continental platforms (hatched curves) is similar to the cratonic profile but with smaller amplitudes ($\overline{\delta T} = -280$ K and $\overline{\delta \mathrm{Fe}} = -2.5\%$ at 100 km depth). Using the same definition as above, the lithosphere would be 190 ± 50 km thick. The bottom parts of our profiles show that at these depths, temperature and iron anomalies are not significant and independent of the surface tectonics.

[28] The temperature and iron perturbations obtained in our study are comparable to those of *Deschamps et al.* [2002], who used a global velocity model. However, our results suggest a cooler and more depleted mantle below the North American craton than the global average values observed in their study ($\delta T = -300$ K and δFe = -3.0% at 100 km depth). Furthermore, we find smaller ranges for temperature and iron variations. The use of a regional tomographic model therefore gives better constraints on these anomalies. Our results also agree well with the study of *Forte and Perry* [2000], who computed thermal and chemical anomalies using different gravity data and global seismic velocity model.

4. Discussion

[29] The distribution of temperature anomalies we obtained (Figure 13) agrees well in general with the work of *Goes and van der Lee* [2002], which is based on inversion of seismic velocities for pure thermal anomalies, and with the work of *Artemieva and Mooney* [2001], which is based on heat flow data. The anomalies of iron (not shown here) are perfectly correlated to the temperature anomalies. This is a consequence of constraining density anomalies with a scaling factor. Of course, additional anomalies of temperature or iron could be present, but we cannot address them, as we do not have full independent information on density. However, the gravity anomalies reconstructed with the correlated part of the density fit the observed gravity anomalies within two standard deviations [*Deschamps et al.*, 2001], suggesting that most of the density anomalies are indeed correlated to the velocity anomalies.

[30] Beneath the Canadian shield and the northern part of the United States, the mantle is significantly colder than average. At z = 100 km, temperature anomalies vary between $\overline{\delta T} = -800$ K and $\overline{\delta T} = -200$ K (Figure 13). The maximum values are observed beneath the Canadian shield and Hudson bay, which were formed during the Precambrian age. The interior platform displays a relatively warmer mantle (~ -300 K). Such lateral variations may be related to geological age and to variations in the lithosphere thickness [*Artemieva and Mooney*, 2001]. Archean and early Proterozoic orogenies modified the shape of the lithosphere, and it is still visible at present day through the action of buoyancy. Another example of age dependence is the feature imaged beneath Greenland, where the cratonic portion (western part) displays a cooler mantle than the platform section (to the east), which correlates well with surface tectonic. *Goes and van der Lee* [2002] suggested that chemical depletion is present in areas where temperatures inferred from P and S wave velocity do not match, such as the North American craton, but they do not give numerical estimates of this depletion. It is worth noting that in our model, these regions show strong iron depletion. As we already mentioned, iron depletion and negative temperature anomalies are correlated. This has some important dynamical consequences. The positive buoyancy induced by chemical depletion may balance the negative buoyancy due to the cooling of the continental root. This may explain the longevity of the Archean craton, by preventing the lithosphere from sinking into the asthenosphere. This hypothesis was formulated quite early [*Jordan*, 1979], but strong observational or numerical evidence is recent [*Forte*

and Perry, 2000; *de Smet et al.*, 2000; *Deschamps et al.*, 2002].

[31] The tectonic Cordillera is underlain by low S velocities following well the tectonic regionalization. It is consistent with an average mantle, and with slightly positive thermal anomalies (δT = 200 K), which are due to the ongoing extension processes occurring in the region.

[32] Using our distribution of temperature and compositional anomalies, we have computed relative v_s and v_p anomalies, and find $\delta lnv_s/\delta lnv_p \simeq 1.7$. Although we used a priori the scaling $\delta lnv_s/\delta lnv_p = 1.6$ to obtain our v_s model, it is reassuring to see that the gravity constraint, via ζ, does not change this ratio very much. More interestingly, most seismological determinations of $\delta lnv_s/\delta lnv_p$ fall within 1.5 ± 0.5 in the uppermost mantle [*Masters et al.*, 2000], and are generally explained by a purely thermal effect with the aid of attenuation [*Karato*, 1993; *Vinnik et al.*, 1999]. We explain the same ratio with a significant contribution from compositional effects, suggesting that $\delta lnv_s/\delta lnv_p$ might not allow to determine the cause of the anomalies unambiguously. The velocities are mainly sensitive to temperature, which does not mean that no significant compositional variations are present.

5. Conclusions

[33] We have inferred variations of temperature and iron in the uppermost mantle beneath North America, using density and S wave velocity perturbations. Density anomalies were estimated from global S wave tomography and gravity anomalies. The regional S wave model is obtained by surface wave tomography and resolves, on the average, lateral structures of 800 km and vertical structures of about 50 km. Our results are in good agreement with previous studies performed at a global scale [*Forte and Perry*, 2000; *Deschamps et al.*, 2002]. In particular, we find that down to a depth of 230 km (±50 km), cratonic roots are significantly colder and depleted in iron, compared to the average mantle. The use of our regional tomographic model improves our image of the thermal and chemical structure of the uppermost mantle, in the sense that ranges of temperature and compositional variations within each major tectonic region are smaller than those observed at a global scale. Next steps will include to refine the distribution of the scaling factor by estimating finer lateral variations of this ratio. In particular, we expect that the depth at which the scaling factor goes to zero vary with the tectonic province. The use of different scaling factors, one for each province, will therefore determine more accurately the depth at which the regional differences in terms of temperature and composition are cancelling.

[34] **Acknowledgments.** This research was founded by the Dutch National Science Foundation (NWO) under grant 750.297.02. We thank E. Humphreys, A. Lenardic, and an anonymous reviewer, whose comments greatly improved the manuscript.

References

Anderson, D. L. (1979), Geophysics of the continental mantle: An historical perspective, in *Continental Mantle*, edited by M. Menzies, pp. 1–30, Clarendon, Oxford, UK.

Artemieva, I. M., and W. D. Mooney (2001), Thermal thickness and evolution of Precambrian lithosphere: A global study, *J. Geophys. Res.*, *106*, 16,387–16,414.

Backus, G. E., and F. Gilbert (1967), The resolving power of gross Earth data, *J. Geophys. Res.*, *16*, 169–205.

Barmin, M. P., M. H. Ritzwoller, and A. L. Levshin (2001), A fast and reliable method for surface wave tomography, *Pure Appl. Geophys.*, *158*, 1351–1375.

Bassin, C., G. Laske, and G. Masters (2000), The current limits of resolution for surface wave tomography in North America, *Eos Trans. AGU*, *81*(48), Abstract S12A-03.

Deschamps, F., R. Snieder, and J. Trampert (2001), The relative density to shear velocity scaling in the uppermost mantle, *Phys. Earth Planet. Inter.*, *124*, 193–211.

Deschamps, F., J. Trampert, and R. Snieder (2002), Anomalies of temperature and iron in the uppermost mantle inferred from gravity data and tomographic models, *Phys. Earth Planet. Inter.*, *129*, 245–264.

de Smet, J. H., A. P. van den Berg, and N. J. Vlaar (2000), Early formation and long-term stability of continents resulting from decompression melting in a convecting mantle, *Tectonophysics*, *322*, 19–33.

Duffy, T. S., and D. L. Anderson (1989), Seismic wave speeds in mantle minerals and the mineralogy of the upper mantle, *J. Geophys. Res.*, *94*, 1895–1912.

Dziewonski, A. M., and D. L. Anderson (1981), Preliminary reference Earth model, *Phys. Earth Planet. Inter.*, *25*, 25,297–25,356.

Ekstrom, G. (2000), Mapping the lithosphere and asthenosphere with surface waves: Lateral structure and anisotropy, in *The History and Dynamics of Global Plate Motions*, *Geophys. Monogr. Ser.*, vol. 121, edited by M. A. Richards, R. G. Gordon, and R. van der Hilst, pp. 239–255, AGU, Washington, D. C.

Forte, A. M., and W. R. Peltier (1991), Viscous flow models of global geophysical observables: 1. Forwards problems, *J. Geophys. Res.*, *96*, 20,131–20,159.

Forte, A. M., and A. C. Perry (2000), Geodynamic evidence for a chemically depleted continental tectosphere, *Science*, *290*, 1940–1944.

Forte, A. M., A. M. Dziewonski, and R. J. O'Connell (1995), Thermal and chemical heterogeneity in the mantle: A seismic and geodynamic study of continental roots, *Phys. Earth Planet. Inter.*, *92*, 45–55.

Goes, S., and S. van der Lee (2002), Thermal structure of the North American uppermost mantle inferred from seismic tomography, *J. Geophys. Res.*, *107*(B3), 2050, doi:10.1029/2000JB000049.

Goes, S., R. Govers, and P. Vacher (2000), Shallow mantle temperatures under Europe from P and S wave tomography, *J. Geophys. Res.*, *105*, 11,153–11,169.

Grand, S. P. (1994), Mantle shear structure beneath the Americas and surrounding oceans, *J. Geophys. Res.*, *99*, 11,591–11,621.

Griffin, W. L., S. Y. O'Reilly, and C. G. Ryan (1999), The composition and origin of sub-continental lithospheric mantle, in *Mantle Petrology: Fields Observations and High-Pressure Experimentation*, edited by Y. Fei, C. M. Bertka, and B. O. Mysen, *Spec. Publ. Geochem. Soc.*, *6*, 13–45.

Hammond, W. C., and E. D. Humphreys (2000), Upper mantle seismic wave velocity: Effects of realistic partial mel geometries, *J. Geophys. Res.*, *105*, 10,975–10,986.

Humphreys, E. D., and K. G. Dueker (1994), Physical state of the western U.S. upper mantle, *J. Geophys. Res.*, *99*, 9635–9650.

Jackson, A. (2000), Laboratory measurement of seismic wave dispersion and attenuation: Recent progress, in *Earth's Deep Interior: Mineral Physics and Tomography from the Atomic to the Global Scale*, *Geophys. Monogr. Ser.*, vol. 117, edited by S. I. Karato et al., pp. 3–26, AGU, Washington, D. C.

Jordan, T. H. (1975), The continental tectosphere: Geophysics and space physics, *Rev. Geophys.*, *13*, 1–12.

Jordan, T. H. (1979), Mineralogies, densities and seismic velocities of garnet lherzolites and their geophysical implications, in *The Mantle Sample: Inclusions in Kimberlites and Other Volcanics*, edited by F. R. Boyd and H. O. A. Myer, pp. 1–14, AGU, Washington, D. C.

Karato, S.-I. (1993), Importance of anelasticity in the interpretation of seismic tomography, *Geophys. Res. Let.*, 1623–1626.

Lemoine, F. G., et al. (1998), The development of the joint NASA/GSFC and National Imagery Mapping Agency (NIMA) geopotential model EGM96, *NASA Tech. Pap., TP-1998-206861*, July.

Masters, G., G. Laske, H. Bolton, and A. Dziewonski (2000), The relative behavior of shear velocity, bulk sound speed, and compressional velocity in the mantle: Implications for chemical and thermal structure, in *Earth's Deep Interior: Mineral Physics and Tomography from the Atomic to the Global Scale*, *Geophys. Monogr. Ser.*, vol. 117, edited by S. I. Karato et al., pp. 63–87, AGU, Washington, D. C.

Mitrovica, J. X., and A. M. Forte (1997), Radial profile of mantle viscosity: Results from the joint inversion of convection and post-glacial rebond observable, *J. Geophys. Res.*, *102*, 2751–2769.

Mooney, W. D., G. Laske, and T. G. Masters (1998), CRUST5.1: A global crustal model at 5° × 5°, *J. Geophys. Res.*, *103*, 727–747.

Nataf, H.-C., and Y. Ricard (1996), 3SMAC: An a priori tomographic model for upper mantle based on geophysical modeling, *Phys. Earth Planet. Inter.*, *95*, 101–122.

Polet, J., and D. L. Anderson (1995), Depth extent of cratons as inferred from tomographic studies, *Geology*, *23*, 205–208.

Pollack, H. N., S. J. Hurter, and J. R. Johnson (1993), Heat flow from the Earth's interior: Analysis of the global data set, *Rev. Geophys.*, 267–280.

Robertson, G. S., and J. H. Woodhouse (1997), Comparison of *P* and *S* station corrections and their relationship to upper mantle structure, *J. Geophys. Res.*, *102*, 27,355–27,366.

Röhm, A., R. Snieder, S. Goes, and J. Trampert (2000), Thermal structure of continental upper mantle inferred from s-wave velocity and surface heat flow, *Earth Planet. Sci. Lett.*, *181*, 396–407.

Rudnick, R., and A. A. Nyblade (1999), The thickness and heat production of Archean lithosphere: Constraints from xenolith thermobarometry and surface heat flow, in *Mantle Petrology: Fields Observations and High-Pressure Experimentation*, edited by Y. Fei, C. M. Bertka, and B. O. Mysen, *Spec. Publ. Geochem. Soc.*, *6*, 3–12.

Schmidberger, S. S., and D. Francis (1999), Nature of the mantle roots beneath the North American craton: Mantle xenolith evidence from Somerset Island kimberlites, *Lithos.*, *48*, 195–216.

Trampert, J., and J. H. Woodhouse (1995), Global phase velocity maps of Love and Rayleigh waves between 40 and 150 seconds, *Geophys. J. Int.*, *122*, 675–690.

Trampert, J., and J. H. Woodhouse (2003), Global anisotropic phase velocity maps for fundamental mode surface waves between 40 and 150 seconds, *Geophys. J. Int.*, *154*, 154–165.

Van der Lee, S., and G. Nolet (1997), Upper mantle *S* velocity structure of North America, *J. Geophys. Res.*, *102*, 22,815–22,838.

Vinnik, L., S. Chevrot, J.-P. Montagner, and F. Guyot (1999), Teleseismic travel time residuals in North America and anelasticity of the asthenosphere, *Phys. Earth Planet. Inter.*, *116*, 93–103.

Woodhouse, J. H., and J. Trampert (1995), Global upper mantle structure inferred from surface wave and body data wave, *Eos Trans. AGU*, *76*(46), Fall Meet. Suppl., F422.

Yan, B., E. K. Graham, and K. P. Furlong (1989), Lateral variations in upper mantle thermal structure inferred from three-dimensional seismic inversion models, *Geophys. Res. Let.*, *16*, 449–452.

F. Deschamps and J. Trampert, Faculty of Earth Sciences, Utrecht University, P.O. Box 80021, 508 TA Utrecht, Netherlands. (deschamp@geo.uu.nl; jeannot@geo.uu.nl)

S. Godey, EMSC, c/o LDG, BP 12, F-91680, Bruyères-le-Châtel, France. (godey@emsc-csem.org)

R. Snieder, Department of Geophysics, Colorado School of Mines, Golden, CO 80401-1887, USA. (rsnieder@mines.edu)